Supporting Information

Multi-layered composites using polyurethane-based foams and 3D-printed structures to curb electromagnetic pollution

Kumari Sushmita [a], *Subhasish Maiti* [b], *Suryasarathi Bose* [b*]

[a] Centre for Nanoscience and Engineering, Indian Institute of Science, Bangalore- 560012, India

[b] Department of Materials Engineering, Indian Institute of Science, Bangalore- 560012, India

***Corresponding author**: sbose@iisc.ac.in

1. Scanning electron micrographs of rGO-Fe_3O_4

Figure S1 shows the low magnification and high magnification scanning electron micrographs of rGO-Fe_3O_4. The rGO-Fe_3O_4 particles were dispersed in THF and drop cast on a silicon wafer, dried, and coated with a few nm of Au before analysis.

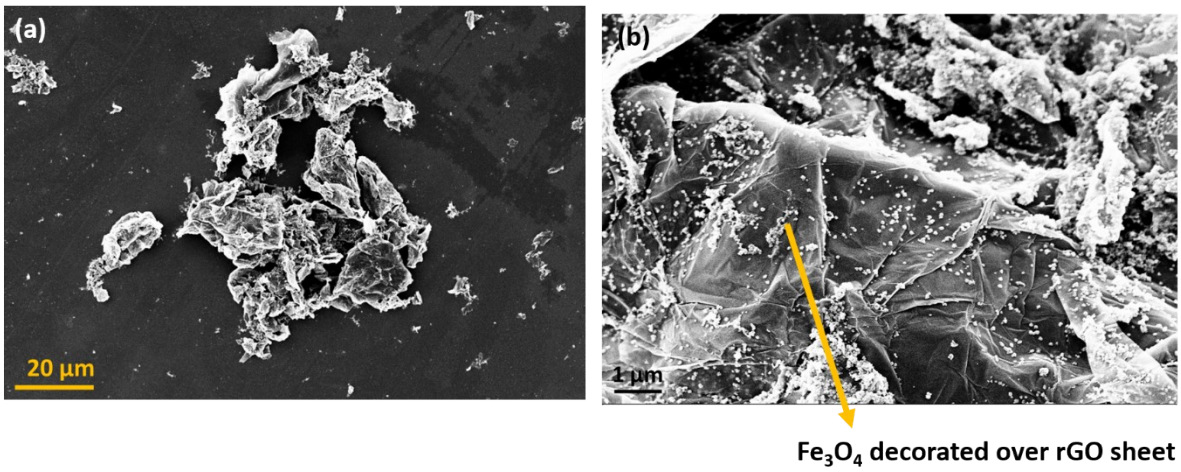

Figure S1: Scanning electron micrographs of rGO-Fe_3O_4: (a) low magnification, (b) high magnification

2. Digital images of the films/foams/3D printed structures

Figures S2a, S2b, and S2c show the digital images of PU film, PU-CNT film, and PU-Ag film, respectively. Figures S2d, S2e and S2f show the digital images of PU foam, PU-CNT foam, and PU-Ag foam, respectively. Figures S2g, S2h, and S2i show the digital images of PU 3Dprint, PU-CNT 3Dprint, and PU-Ag 3Dprint, respectively. As can be observed in figures

S2c, S2f, and S2i, Ag sputter deposition was done on one of the surfaces of the PU-based structures.

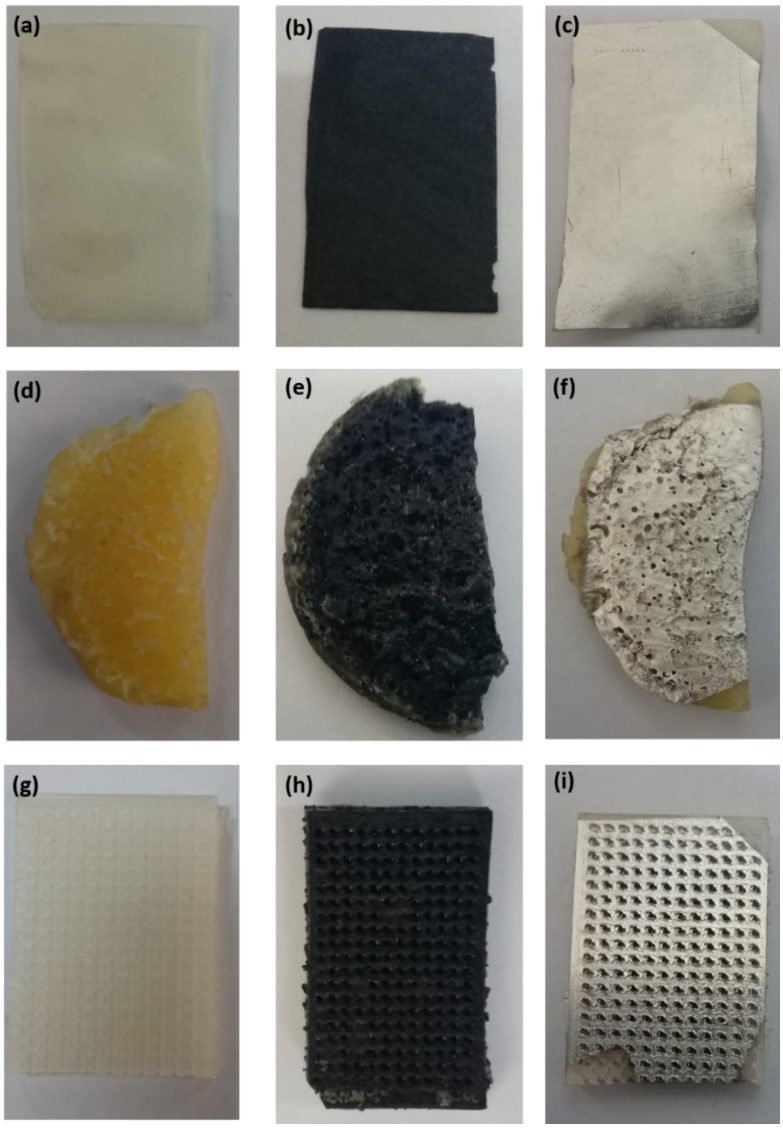

Figure S2: Digital images of (a) PU film, (b) PU-CNT film, (c) PU-Ag film, (d) PU foam, (e) PU-CNT foam, (f) PU-Ag foam, (g) PU 3Dprint, (h) PU-CNT 3Dprint and (i) PU-Ag 3Dprint.

Figures S3a and S3b show the PC-CNT film and PVDF-rGO-Fe_3O_4 film, respectively. PVDF is a film-forming polymer and can incorporate high content of fillers. However, incorporating 3 wt% of CNT in PC (a brittle polymer) improves the flexibility of the film. This is evident from figure S3a, where PC seems to bend without fracture.

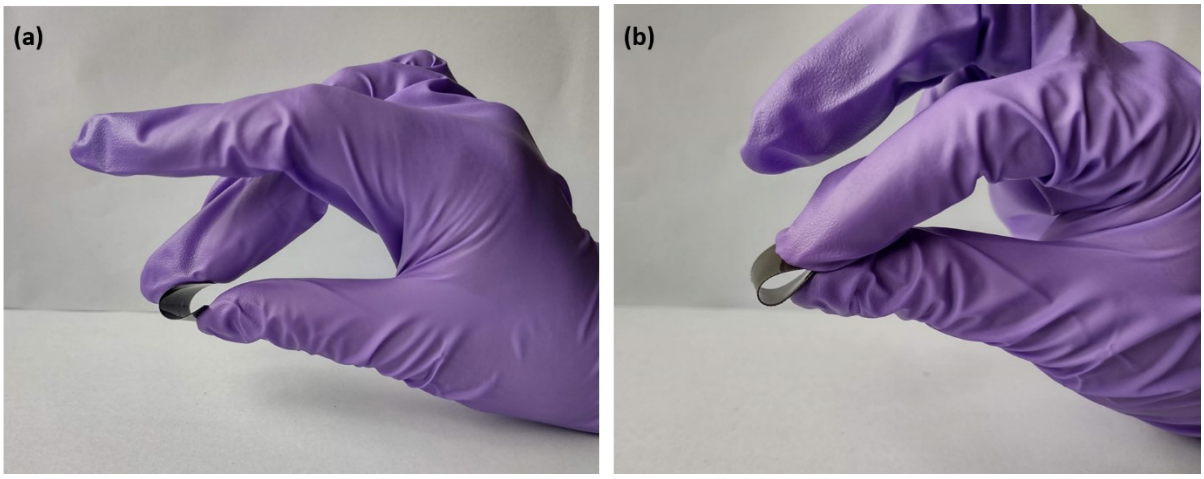

Figure S3: Digital images of (a) PC-CNT film and (b) PVDF-rGO-Fe_3O_4 film

Figure S4 shows the digital images of PC-CNT film and PU-CNT films. As can be observed from these images, the PC-CNT film shows a more uniform film than the PU-CNT film, where dark and bright patches can be observed even at the macro level. This can be one of the major reasons why PC-CNT film shows a higher electrical conductivity than PU-CNT film.

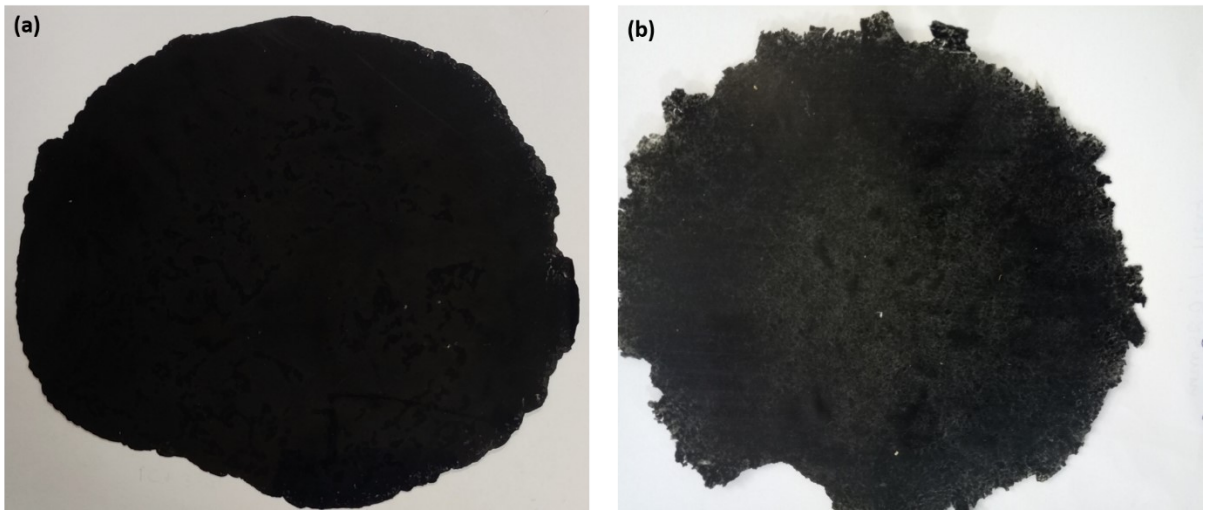

Figure S4: Digital images of (a) PC-CNT film, (b) PU-CNT film

3. Scanning electron micrographs of PU-based structures

The SEM of PU-CNT foam and PU-CNT 3Dprint are shown in figures S5a and S5b, respectively. PU-CNT foam has more non-uniform (in size especially) dead pores compared to PU-CNT 3D printed structure.

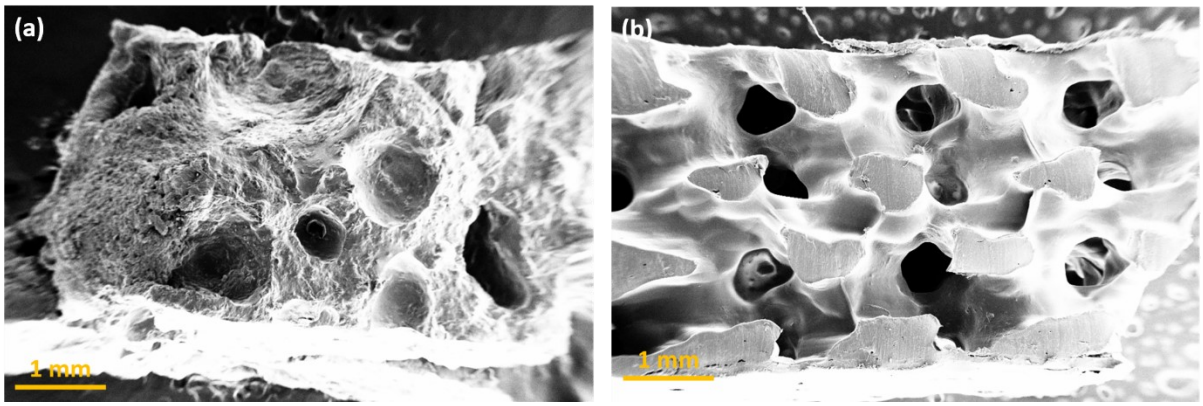

Figure S5: SEM of (a) PU-CNT foam, (b) PU-CNT 3Dprint

4. Morphological analysis of multi-layered structures

Figure S6 shows the SEM and EDS mapping of PVDF/PU film/PC. As shown in figure S6b, carbon can be found throughout the multi-layered film because of the carbon present in all the three polymers, i.e., PVDF, PU, and PC. Oxygen is present in PU and PC, and it can be observed that oxygen concentration is more towards the bottom layers (refer to figure S6c). F and Fe are found in the top layer, as observed in figures S6d and S6e, suggesting that the top layer is PVDF filled with rGO-Fe_3O_4.

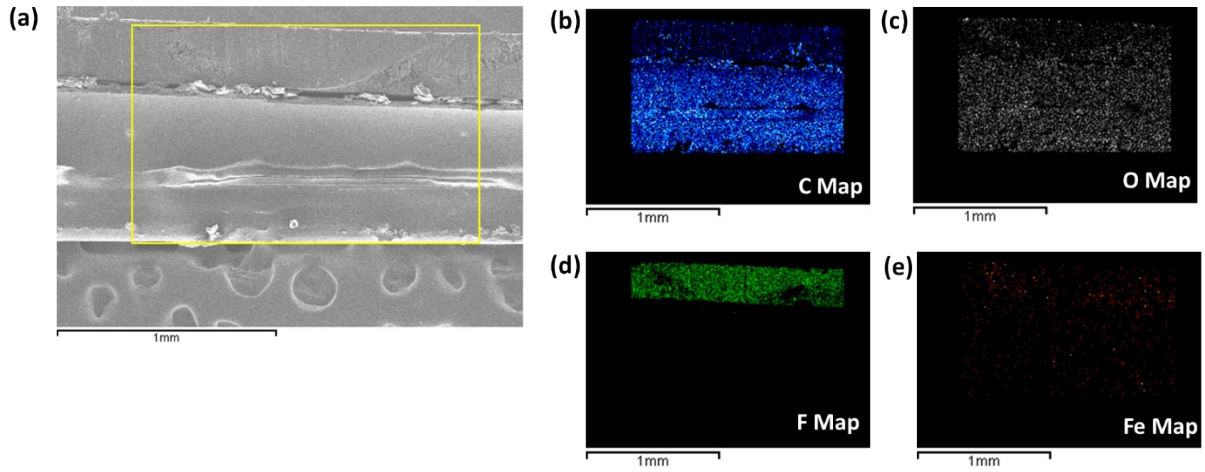

Figure S6: (a) Scanning electron micrograph of PVDF/PU film/PC under consideration for EDS analysis, (b) EDS mapping: C map, (c) EDS mapping: O map, (d) EDS mapping: F map, (e) EDS mapping: Fe map.

Figure S7 and S8 show the SEM and EDS mapping of the top, middle, and bottom portions of PVDF/PU foam/PC and PVDF/PU 3Dprint/PC, respectively. The cross-sectional size of the multi-layered structure was about 5.3 mm, which required a higher working distance to keep the entire sample in focus, leading to extremely poor signal detection of various elements during mapping. Hence, the EDS mapping of different portions in the multi-layered structure

was done separately. The "a, b, and c series" in figures S7 and S8 show the top, middle, and bottom portions of the two different multi-layered structures. It is evident from the mapping that the top portion in both figures S7 and S8 is the PVDF-rGO-Fe_3O_4 film due to the high concentration of F detected in those regions. Even the presence of Fe can be observed in figure S7 a5 and figure S8 a5. The middle layer is the porous PU, followed by the bottommost layer as PC composite film. These two layers cannot be differentiated through EDS, as both PC and PU contain C and O in their main backbone chain. The outer flat sheets of PC-CNT film and PVDF-rGO-Fe_3O_4 film act as a support layer holding the porous structure intact.

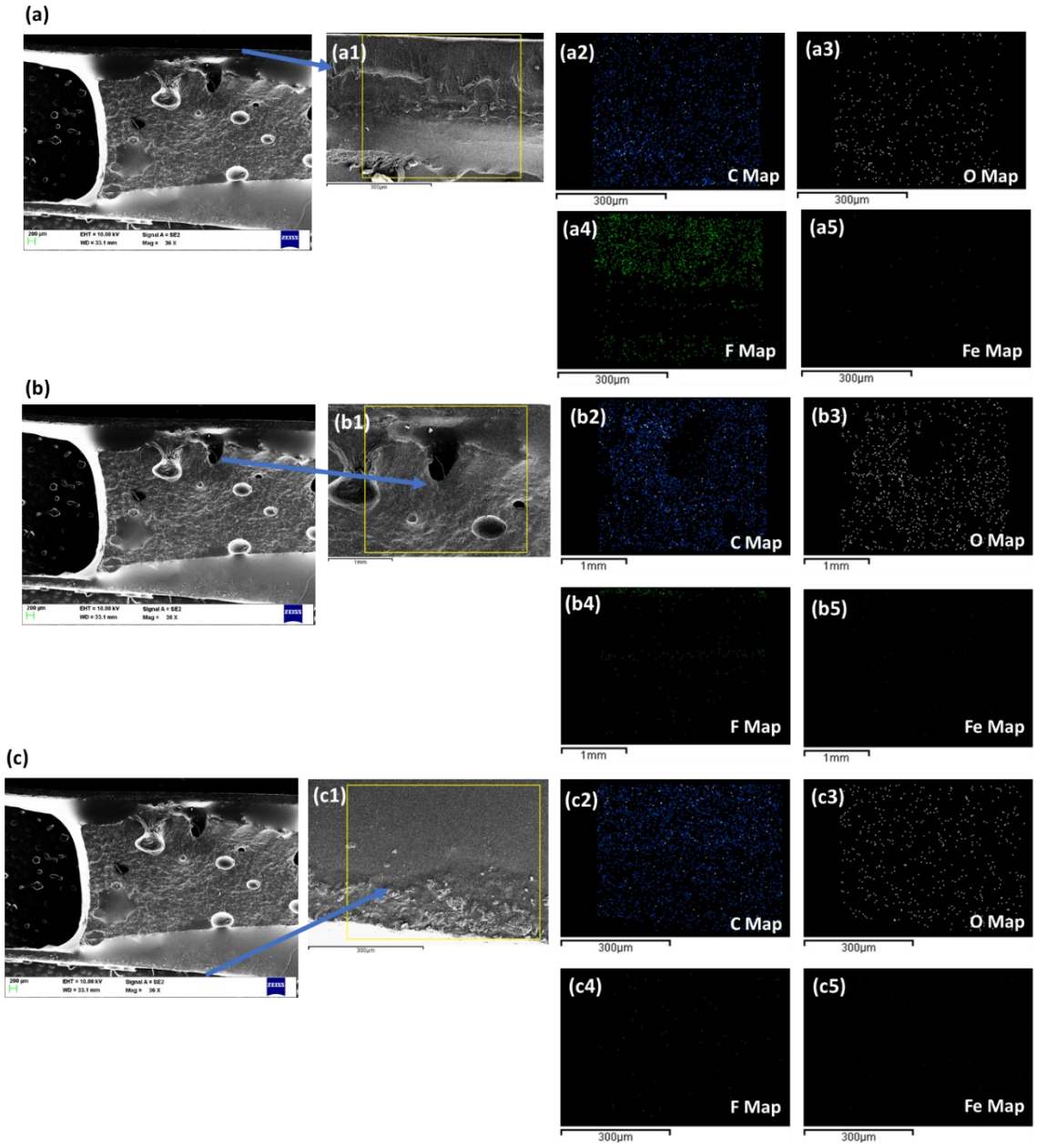

Figure S7: (a, b, c) Scanning electron micrograph of PVDF/PU foam/PC; (a1) The scanning electron micrograph of the top portion (of figure a) under consideration for EDS analysis, (a2) EDS mapping (for

area in a1): C map, (a3) EDS mapping (for area in a1): O map, (a4) EDS mapping (for area in a1): F map, (a5) EDS mapping (for area in a1): Fe map; (b1) The scanning electron micrograph of the middle portion (of figure b) under consideration for EDS analysis, (b2) EDS mapping (for area in b1): C map, (b3) EDS mapping (for area in b1): O map, (b4) EDS mapping (for area in b1): F map, (b5) EDS mapping (for area in b1): Fe map; (c1) The scanning electron micrograph of the bottom portion (of figure c) under consideration for EDS analysis, (c2) EDS mapping (for area in c1): C map, (c3) EDS mapping (for area in c1): O map, (c4) EDS mapping (for area in c1): F map, (c5) EDS mapping (for area in c1): Fe map

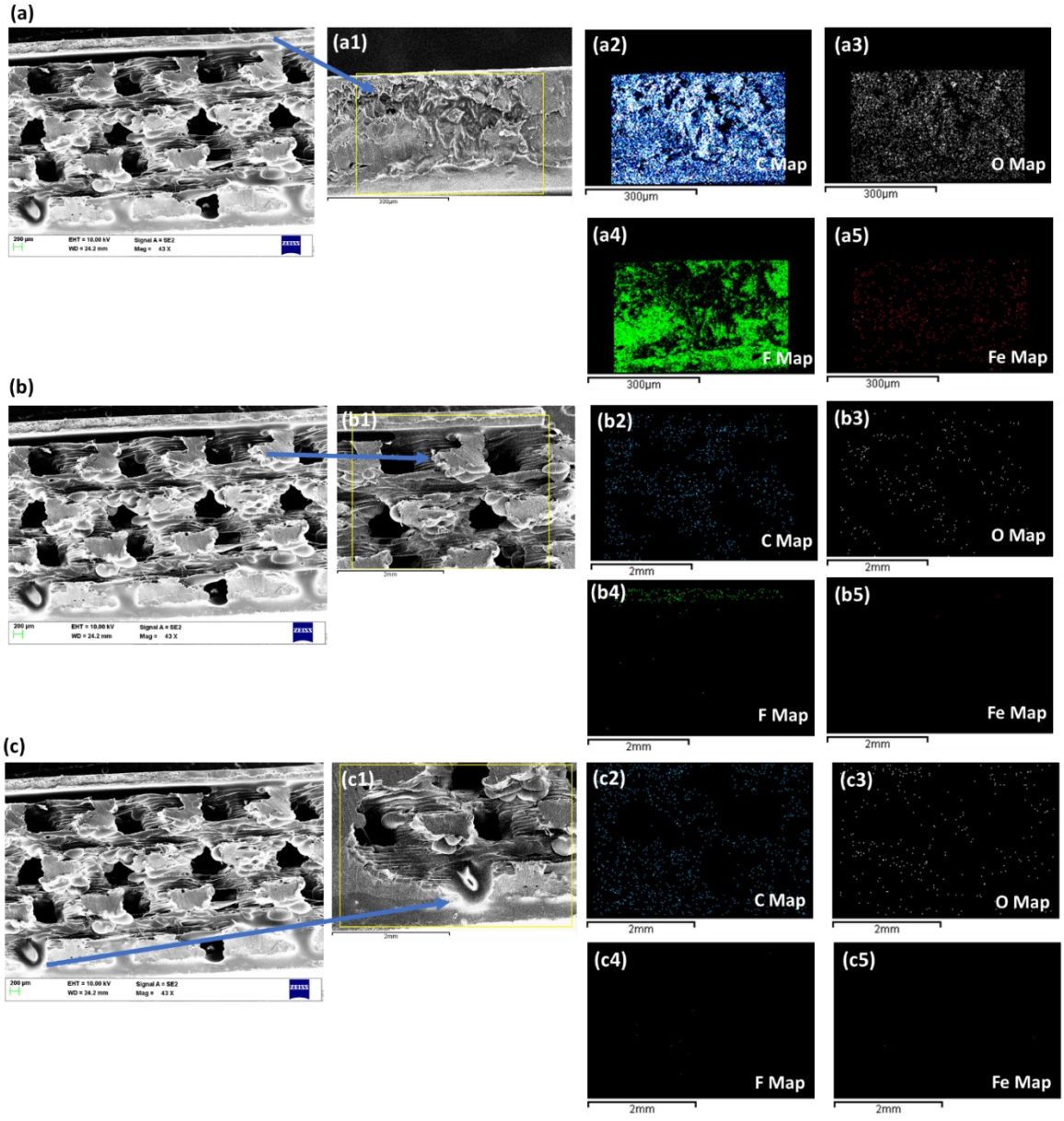

Figure S8: (a, b, c) Scanning electron micrograph of PVDF/PU 3Dprint/PC; (a1) The scanning electron micrograph of the top portion (of figure a) under consideration for EDS analysis, (a2) EDS mapping (for area in a1): C map, (a3) EDS mapping (for area in a1): O map, (a4) EDS mapping (for area in a1): F map, (a5) EDS mapping (for area in a1): Fe map; (b1) The scanning electron micrograph of the middle portion (of figure b) under consideration for EDS analysis, (b2) EDS mapping (for area in b1): C map, (b3) EDS mapping (for area in b1): O map, (b4) EDS mapping (for area in b1): F map, (b5) EDS mapping (for area

in b1): Fe map; (c1) The scanning electron micrograph of the bottom portion (of figure c) under consideration for EDS analysis, (c2) EDS mapping (for area in c1): C map, (c3) EDS mapping (for area in c1): O map, (c4) EDS mapping (for area in c1): F map, (c5) EDS mapping (for area in c1): Fe map

5. Porosity of the foams and 3D printed structures

The total porosity of the foam was assessed using the Archimedes method as reported in literature [1, 2]. Water was used as the liquid medium. The porosity of porous structures was obtained using equation 1.

$$\% \text{ Porosity} = \frac{(Wsaturated - Wdry)}{(Wsaturated - Wsuspended)} * 100 \text{ ----------(1)}$$

Where $Wdry$ is the dry weight of the porous structure, $Wsaturated$ is the weight of porous structure saturated with water, and $Wsuspended$ is the weight of porous structure suspended in water.

Table S1: The porosity of PU-based foams and 3D printed structures.

	$Wsaturated$	$Wdry$	$Wsuspended$	**% Porosity**
PU foam	350 mg	180 mg	100 mg	68 %
PU-CNT foam	360 mg	290 mg	260 mg	70 %
PU 3D print	150 mg	110 mg	80 mg	57.1 %
PU-CNT 3D print	160 mg	90 mg	40 mg	58.3%

The porosity of foam-based structures is found to be higher than the 3D printed structures. This may be because of the continuous tortuous pores in 3D printed structures compared to the dead pores in foams. The latter retained more water within their structures.

6. EMI shielding performance and mechanism study

Figure S9 shows the SE_T vs. frequency and absorption-reflection plot of PU block based-single layered and multi-layered structures. It is to be noted that PU block (or PU-CNT block) is the control specimen (non-porous) and has a thickness same as PU foam (or PU-CNT foam) and PU 3D print (or PU-CNT 3Dprint) structures.

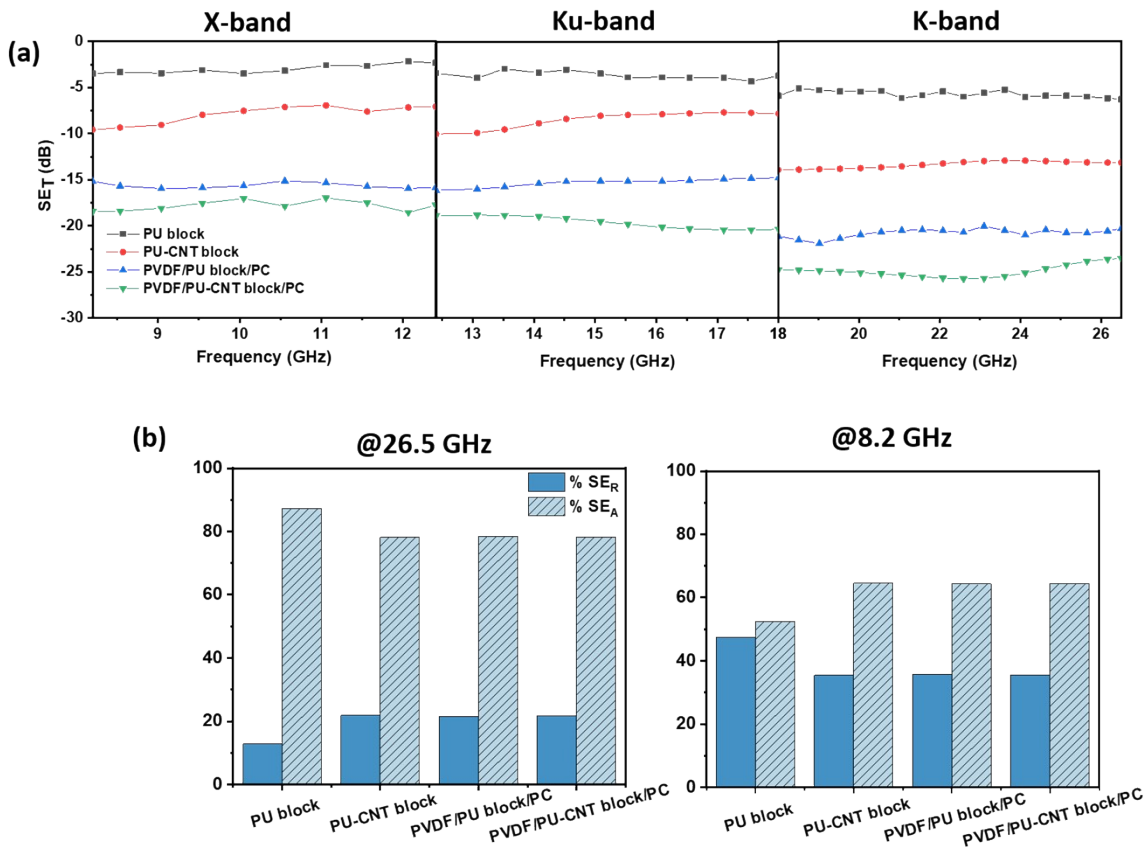

Figure S9: PU-block based single-layered and multi-layered structures (control sample) (a) SE_T vs. frequency plots, (b) % SE_A (the light blue bar with stripe pattern) and % SE_R (the dark blue bar with no pattern) at 26.5 and 8.2 GHz.

Figure S10a shows the SE_T vs. frequency plots of the PC-CNT film and PVDF-rGO-Fe_3O_4 film in X-, Ku-, and K-band. These films serve as the outer sheet layer in the multi-layered structure. PC-CNT film shows the SE_T of ~-12 dB, whereas the PVDF-rGO-Fe_3O_4 film shows the SE_T of ~-6 dB.

Further, the dielectric and magnetic parameters were evaluated to understand the intrinsic reason for the absorption/reflection-based shielding. Figure S10b shows the permittivity (ε', ε'') and permeability (μ', μ'') for the PC-CNT and PVDF-rGO-Fe_3O_4 at 26.5 GHz frequency. These values were calculated using the Nicholson Ross Weir algorithm, which derives the material property from the scattering parameters. ε' and μ' are the real part of complex relative permittivity and permeability, respectively. It is a measure of how much energy from an external field is stored in a material. ε'' and μ'' are the imaginary part of complex relative permittivity and permeability, respectively, and is called the loss factor. It is a measure of how dissipative or lossy a material is to an external field. Since the response of a material to the

alternating electric field and the magnetic field is not instantaneous, there exists a phase lag. The tangent of this phase angle is tan δ or loss tangent which is used to express the relative losses incurred by material, and it is defined as:

$$\tan \delta\varepsilon = \frac{\varepsilon''}{\varepsilon'}, \quad \tan \delta\mu = \frac{\mu''}{\mu'} \qquad \text{----------(2)}$$

The total relative loss is represented as a summation of tan δε (dielectric loss factor) and tan δμ (magnetic loss factor). It is a measure of the overall lossy nature of a material. Figure S10c shows the bar plot of tan δε, tan δμ, and (tan δε + tan δμ) for the PC-CNT and PVDF-rGO-Fe_3O_4 at 26.5 GHz frequency. This plot suggests that dielectric loss is higher for PC-CNT than PVDF-rGO-Fe_3O_4, which can be attributed to the highly conducting CNTs leading to the polarization losses, conduction losses, and eddy current losses [3, 4]. As Fe_3O_4 is a ferrimagnetic material, PVDF-rGO-Fe_3O_4 showed a higher magnetic loss than PC-CNT. But when we consider the summation of tan δε and tan δμ, PVDF-rGO-Fe_3O_4 exhibits a higher value, confirming the lossy character of rGO-Fe_3O_4.

Microwave absorption properties of polymer composites can be explained through the impedance matching performance and attenuation constant (α). Electromagnetic impedance matching requires that the shield satisfy the criteria of $|Z_{in}/Z_0|$ equal or close to 1.0 [5]. The $|Z_{in}/Z_0|$ values were calculated using equation 3.

$$\left|\frac{Z_{in}}{Z_0}\right| = \sqrt{\frac{\mu_r}{\varepsilon_r}} \tanh\left\{j\left(\frac{2\pi f d}{c}\right)\sqrt{\mu_r \varepsilon_r}\right\} \qquad \text{----------(3)}$$

where Z_{in} is the input characteristic impedance of the shield, Z_0 is the characteristic impedance of free space, ε_r refers to the complex relative permittivity of the shield material, μ_r refers to the complex relative permeability of the shield material, f is the frequency of incident EM wave, d is the thickness of the shield, and c is the velocity of light in vacuum.

The attenuation constant determines how well the penetrating EM wave will be rapidly attenuated or suffer decay [6, 7]. The attenuation constant can be calculated using equation 4.

$$\alpha = \frac{\sqrt{2}\,\pi f}{c} \times \sqrt{(\mu''\varepsilon'' - \mu'\varepsilon') + \sqrt{(\mu''\varepsilon'' - \mu'\varepsilon')^2 + (\mu'\varepsilon'' - \mu''\varepsilon')^2}} \qquad \text{----------(4)}$$

As observed from figures S10c, the $|Z_{in}/Z_0|$ is approx. 0.1 (@26.5 GHz), suggesting a poor impedance match exhibited by PC-CNT and PVDF-rGO-Fe_3O_4. However, it is worthwhile

noting that the impedance match is slightly higher (depicted by a higher value of $|Z_{in}/Z_0|$) for PVDF-rGO-Fe_3O_4 than PC-CNT. Since CNTs are conducting, the impedance mismatch is comparatively higher in composites with CNTs than that with rGO-Fe_3O_4. The latter has more lossy characteristics, as is also depicted by the higher value of (tan δε + tan δμ). The α value (refer to figure S10d) is higher in the case of PC-CNT, suggesting a rapid attenuation of EM wave, as is also concluded from the higher SE_T value of PC-CNT compared to PVDF-rGO-Fe_3O_4.

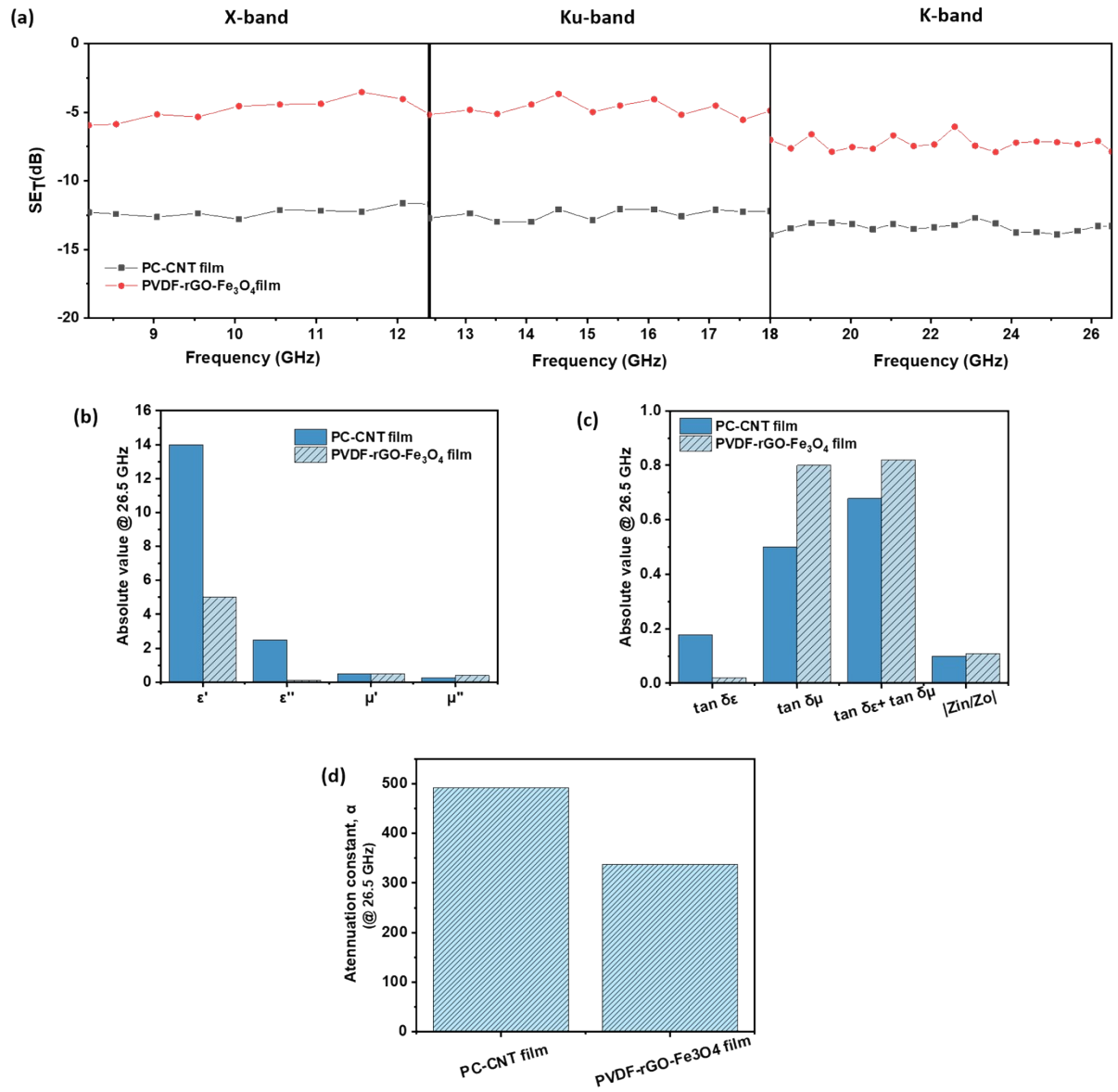

Figure S10: (a) SE_T vs. frequency of PC-CNT film and PVDF-rGO-Fe_3O_4 film, (b) real and imaginary component of permittivity and permeability for PC-CNT and PVDF-rGO-Fe_3O_4 at 26.5 GHz frequency, (c) tan δε, tan δμ, total tan δ, and impedance match characteristics of PC-CNT and PVDF-rGO-Fe_3O_4 at 26.5 GHz frequency, (d) attenuation constant of PC-CNT and PVDF-rGO-Fe_3O_4 at 26.5 GHz frequency.

Further, the underlying mechanism of multi-layered structures with the highest SE_T values (two samples chosen-one with Ag layer and the other without Ag layer) was studied with respect to the control sample at 26.5 GHz frequency (refer to figure S11). The permittivity (ε', ε'') and permeability (μ', μ'') for the best (PVDF/PU-CNT foam/PC and PVDF/PU-Ag foam/PC) and control (PVDF/PU-CNT block/PC) samples are shown in figure S11a. The Ag-based samples have higher permittivity values owing to their highly conducting nature. The tanδ values for the best and control samples are shown in figure S11b. The ($\tan \delta\varepsilon + \tan \delta\mu$) is found to be highest for the multi-layered structure with PU-CNT foam and lowest for the control sample. The interconnected conductive network conducts charge through hoping inside the porous matrix, generating very high conduction losses. In addition, the eddy current losses exist due to the presence of these conducting fillers. The lattice mismatch between the rGO sheet and Fe_3O_4 creates abundant interfaces that act as areas of charge accumulation that form capacitor-like junctions that contribute to an increase in dielectric storage properties [6]. This charge accumulation acts as electric dipoles, interacting and diminishing the electric component of the EM wave. Moreover, the heterogeneous nature of the structure and the multiple air traps in foam also serve as regions for charge accumulation (because of the different dielectric properties of materials on either side of the interface), which act as a barrier to charge transfer during the electrical conduction process. The wave considerably loses power as it tries to hop or tunnel through these dielectrically different components. The multiple interfaces between filler-polymer, polymer-air traps, and polymer-polymer result in EM attenuation and manifest as absorption. The lower value of total tan δ of the control sample also suggests that the porosity enhances the absorption-based EMI shielding performance. The impedance match characteristic of the samples (refer to figure S11c) depicts that the match is slightly lower for PVDF/PU-Ag foam/PC and the highest for PVDF/PU-CNT foam/PC. The presence of highly conducting Ag in the inside layer possibly results in a lower impedance match. However, comparing the values of impedance match in figures S10c and S11c, the multi-layered structures show an enhanced impedance match suggesting higher absorption-based shielding than conventional composites. The values of the attenuation constant (refer to figure S11d) further depict that the porous multi-layered structures show the highest values compared to the non-porous multi-layered structure. Since skin depth (refer to figure S11e) is inversely proportional to SE_A, it is lowest for PVDF/PU-CNT foam/PC and highest for PVDF/PU-CNT block/PC. A lower value of skin depth indicates that the intensity of incoming EM wave drops to 1/e at a lower shield thickness.

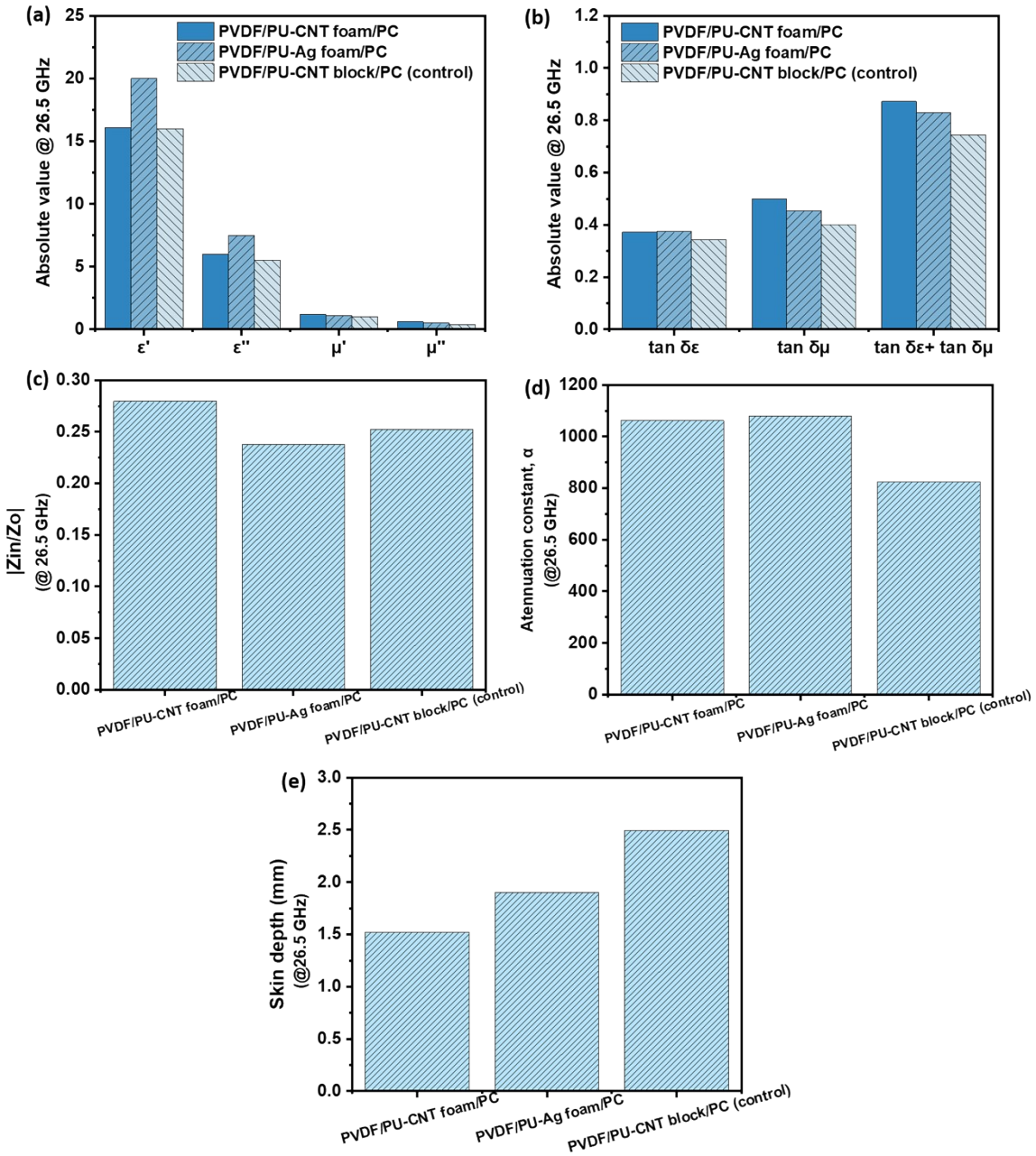

Figure S11: (a) Real and imaginary components of permittivity and permeability for best samples vs. control sample at 26.5 GHz frequency, (b) tan δε, tan δμ, and total tan δ for best samples vs. control sample at 26.5 GHz frequency, (c) impedance match characteristics for best samples vs. control sample at 26.5 GHz frequency, (d) attenuation constant for best samples vs. control sample at 26.5 GHz frequency, (e) skin depth for best samples vs. control sample at 26.5 GHz frequency,

Tables S2 and S3 show the SE_T and % absorption data of the relevant single-layered and multi-layered structures, respectively.

Table S2: Key outcomes (in terms of EMI shielding performance) of the single-layered PU structures.

PU-based structure	Highest SE_T obtained (in dB) (in the range of 8.2-26.5 GHz)	% Absorption at 8.2 GHz or 26.5 GHz (minimum of the two taken)
PU film	-2 (negligible)	-
PU foam	-10	69 %
PU 3Dprint	-6	73 %
PU block	-6	52%
PU-CNT film	-7	59%
PU-CNT foam	-30	89%
PU-CNT 3Dprint	-12	74%
PU-CNT block	-14	64%
PU-Ag film	-48	58%
PU-Ag foam	-34	75%
PU-Ag 3Dprint	-39	75%
PU-CNT-Ag foam	-36	86%
The thickness of single-layered PU-based film ~ 0.3 mm, the thickness of PU-based foam/3D print/block ~ 4.7 mm		

Table S3: Key outcomes (in terms of EMI shielding performance) of the multi-layered configurations

Multi-layered structure's configuration	Highest SE_T obtained (in dB) (in the range of 8.2-26.5 GHz)	% Absorption at 8.2 GHz or 26.5 GHz (minimum of the two taken)
PVDF/PU foam/PC	-25	92 %
PVDF/PU 3Dprint /PC	-24	90 %
PVDF/PU block /PC	-22	64 %
PVDF/PU-CNT film/PC	-18	76 %
PVDF/PU-CNT foam/PC	-39	91 %
PVDF/PU-CNT 3Dprint/PC	-27	92 %
PVDF/PU-CNT block/PC	-26	64 %
PVDF/PU-Ag film/PC	-47	72 %
PVDF/PU-Ag foam/PC	-50	73 %
PVDF/PU-Ag 3Dprint/PC	-42	68 %
PVDF/PU-CNT-Ag foam/PC	-45	70 %
The thickness of multi-layered structure with PU-based film ~1 mm, the thickness of multi-layered structure with PU-based foam/3D print ~ 5.3 mm		

Figure S12 shows the overall EMI Shielding performance of the multi-layered configurations with PU-CNT-based, PU-Ag-based, and PU-CNT-Ag-based structures.

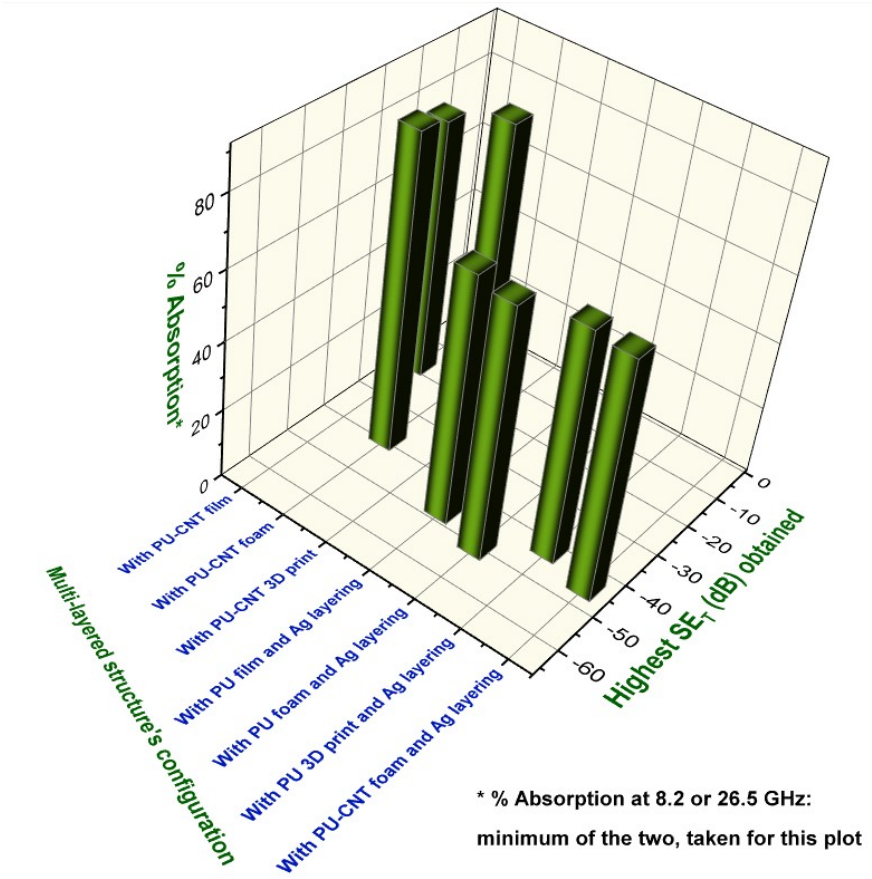

Figure S12: EMI Shielding performance of the multi-layered configurations with PU-CNT-based structures, PU-Ag-based structures, and PU-CNT-Ag-based structures.

References

1. S. Fu, W. Liu, S. Liu, S. Zhao and Y. Zhu, *Science and Technology of Advanced Materials*, 2018, **19**, 495-506.
2. S. T. AbdulQader, I. A. Rahman, H. Ismail, T. Ponnuraj Kannan and Z. Mahmood, *Ceramics International*, 2013, **39**, 2375-2381.
3. G. J. H. Melvin, Q.-Q. Ni, Y. Suzuki and T. Natsuki, *Journal of Materials Science*, 2014, **49**, 5199-5207.
4. J. Sun, W. Wang and Q. Yue, *Materials*, 2016, **9**, 231.
5. Z. Zhang, X. Chen, Z. Wang, L. Heng, S. Wang, Z. Tang and Y. Zou, *Opt. Mater. Express*, 2018, **8**, 3319-3331.
6. A. V. Menon, B. Choudhury, G. Madras and S. Bose, *Chem. Eng. J.*, 2020, **382**, 122816.
7. S. P. Pawar, V. Bhingardive, A. Jadhav and S. Bose, *RSC Advances*, 2015, **5**, 89461-89471.